Atmos. Chem. Phys. Discuss., 11, 341–386, 2011
www.atmos-chem-phys-discuss.net/11/341/2011/
doi:10.5194/acpd-11-341-2011

Atmospheric Chemistry and Physics Discussions

Optimizing global CO emissions using a four-dimensional variational data assimilation system and surface network observations

P. B. Hooghiemstra[1,2], M. C. Krol[1,2,3], J. F. Meirink[4], P. Bergamaschi[5], G. R. van der Werf[6], P. C. Novelli[7], I. Aben[2,6], and T. Röckmann[1]

[1]Institute for Marine and Atmospheric Research Utrecht, University of Utrecht, Utrecht, The Netherlands
[2]Netherlands Institute for Space Research (SRON), Utrecht, The Netherlands
[3]Wageningen University and Research Centre, Wageningen, The Netherlands
[4]Royal Netherlands Meteorological Institute (KNMI), de Bilt, The Netherlands
[5]European Commission Joint Research Centre, Institute for Environment and Sustainability, Ispra, Italy
[6]Faculty of Earth and Life Sciences, VU University, Amsterdam, The Netherlands
[7]Global Monitoring Division, Earth System Research Laboratory, NOAA, Boulder, Colorado, USA

Received: 8 October 2010 – Accepted: 13 December 2010 – Published: 6 January 2011

Correspondence to: P. Hooghiemstra (p.b.hooghiemstra@uu.nl)

ACPD
11, 341–386, 2011

Abstract

We apply a four-dimensional variational (4D-VAR) data assimilation system to optimize carbon monoxide (CO) emissions for 2003 and 2004 and to reduce the uncertainty of emission estimates from individual sources using the chemistry transport model TM5. The system is designed to assimilate large (satellite) datasets, but in the current study only a limited amount of surface network observations from the National Oceanic and Atmospheric Administration Earth System Research Laboratory (NOAA/ESRL) Global Monitoring Division (GMD) is used to test the 4D-VAR system. By design, the system is capable to adjust the emissions in such a way that the posterior simulation reproduces background CO mixing ratios and large-scale pollution events at background stations. Uncertainty reduction up to 60% in yearly emissions is observed over well-constrained regions and the inferred emissions compare well with recent studies. However, with the limited amount of data from the surface network, the system becomes data sparse. This results in a large solution space and the 4D-VAR system has difficulties in separating anthropogenic and biogenic sources in particular. In addition we show that uncertainties in the model such as biomass burning injection height and the OH distribution largely influence the inversion results. The inferred emissions are validated with NOAA aircraft data over North America and the agreement is significantly improved from prior to posterior simulation. Validation with the Measurements Of Pollution In The Troposphere (MOPITT) instrument version 4 (V4) shows only a slight improved agreement over the well-constrained Northern Hemisphere. However, the model with optimized emissions underestimates MOPITT CO total columns on the remote Southern Hemisphere (SH) by about 40%. This is caused by a reduction in SH CO sources mainly due to surface stations on the high southern latitudes.

ACPD
11, 341–386, 2011

1 Introduction

Understanding the budget of carbon monoxide (CO) is important, because by reaction with the radical OH, CO influences the oxidizing capacity of the atmosphere significantly (Logan et al., 1981). Enhanced CO concentrations reduce OH concentrations and this has a feedback on the concentration of methane, the second most important anthropogenic greenhouse gas. CO is also a precursor of tropospheric ozone under high NO_x ($NO+NO_2$) conditions (Seinfeld and Pandis, 2006). CO is emitted into the atmosphere by incomplete combustion of fossil fuels, biofuels and during biomass burning events. In addition, CO is produced throughout the atmosphere by oxidation of methane and non-methane volatile organic compounds (NMVOCs). The main sink of CO is the reaction with the OH radical, the so-called cleansing agent of the atmosphere (Logan et al., 1981). Deposition of CO on the Earth's surface is a minor sink, accounting for 5–10% of the total sink strength (Sanhueza et al., 1998; Pétron et al., 2002).

The magnitude of CO emissions from different source categories is not well quantified. In particular, emissions from biomass burning (most importantly forest and savanna fires) carry large uncertainties partly due to the variability of fires in both space and time. In addition, bottom-up inventories like the widely used Global Fire Emission Database (GFED) (van der Werf et al., 2004, 2006, 2010) come with substantial uncertainties due to insufficient knowledge about burned area, fuel load, and emission factors (van der Werf et al., 2006). Uncertainties in biomass burning emission estimates are largest in deforestation regions (e.g., South America and Indonesia) and regions where organic soils burn (e.g., Indonesia and the Boreal region).

One way to better constrain emissions of CO is inverse modeling (Enting, 2002). In short, atmospheric measurements, a chemistry transport model (CTM) and a priori information about the emissions are used to optimize the emission in such a way that the mismatch between simulated and observed CO concentrations is minimized. The a priori emission estimates are taken from bottom-up inventories. Throughout the lit-

ACPD
11, 341–386, 2011

erature there are basically two inversion methods used for CO inversions: Synthesis Bayesian inversions (e.g., Bergamaschi et al., 2000; Kasibhatla et al., 2002; Pétron et al., 2002; Palmer et al., 2003, 2006; Arellano et al., 2004, 2006; Heald et al., 2004; Jones et al., 2009) and adjoint inversions (e.g., Müller and Stavrakou, 2005; Yumimoto and Uno, 2006; Stavrakou and Müller, 2006; Chevallier et al., 2009; Kopacz et al., 2009, 2010; Fortems-Cheiney et al., 2009; Tangborn et al., 2009). The synthesis inversion optimizes CO emissions over large geographical regions with a preset CO emission distribution in each region, whereas the adjoint inversion technique is capable to derive optimized CO emissions on the grid-scale of the underlying CTM, thereby reducing the risk of aggregation errors (Kaminski et al., 2001). An iterative approach is used to minimize the mismatch between model and observations. Adjoint inversions are in particular suited for assimilation of large observational (satellite) datasets (Bergamaschi et al., 2009; Meirink et al., 2008b).

In the current study we apply a 4D-VAR system for CO based on the earlier work for methane (Meirink et al., 2008a,b; Bergamaschi et al., 2009). Although this system is designed to assimilate large amounts of observational data, it will be tested in this first study by only assimilating surface observations from a limited number of NOAA stations to optimize monthly mean CO emissions for a period of two years. This approach is followed to obtain a benchmark characterization of the system for future assimilation of satellite data. Firstly, we focus on the capability of the system to estimate annual continental emissions by inspecting the reduction of the prior errors that are set on the sources. The optimized emissions will be validated by comparing model results to independent aircraft data from NOAA and satellite data from the Measurements Of Pollution in The Troposphere (MOPITT) instrument (Deeter et al., 2003, 2007, 2010). Secondly, we will investigate the influence of prior settings and model errors on the inversion results by performing sensitivity studies.

This paper is organized as follows: The 4D-VAR system is described in Sect. 2. Section 3 presents the optimized (posterior) emissions and their uncertainty reduction for 2003 and 2004 as well as a validation with independent aircraft and satellite data. The

ACPD
11, 341–386, 2011

results are discussed in Sect. 4 and the performance of the 4D-VAR system is further investigated by performing sensitivity studies (Sect. 5). Finally we give conclusions in Sect. 6.

2 Description of the four dimensional variational data assimilation system

The 4D-VAR modeling system for CO is based on the TM5-4DVAR system originally developed for methane (Meirink et al., 2008b; Bergamaschi et al., 2009). Given a set of atmospheric observations $\boldsymbol{y}$ and a chemistry transport model H it is possible to optimize a set of fluxes $\boldsymbol{x}$ (the state vector) using the Bayesian technique (Rodgers, 2000). The a posteriori vector $\boldsymbol{x}$ is found by minimizing the mismatch between the model forward simulation $H(\boldsymbol{x})$ and the observations ($\boldsymbol{y}$) weighted by an observation error covariance matrix $\mathbf{R}$ while staying close to a set of a priori fluxes $\boldsymbol{x}_b$, weighted with the a priori error covariance matrix $\mathbf{B}$. Mathematically this problem can be written as the following minimization problem:

$$\hat{\boldsymbol{x}} = \text{Argmin}\, \mathcal{J} \tag{1}$$

$$\mathcal{J}(\boldsymbol{x}) = \frac{1}{2}(\boldsymbol{x}-\boldsymbol{x}_b)^{\mathrm{T}}\mathbf{B}^{-1}(\boldsymbol{x}-\boldsymbol{x}_b) + \frac{1}{2}\sum_{i=1}^{n}(H_i(\boldsymbol{x})-\boldsymbol{y}_i)^{\mathrm{T}}\mathbf{R}_i^{-1}(H_i(\boldsymbol{x})-\boldsymbol{y}_i), \tag{2}$$

where the index i refers to the time step and T is the transpose operator. Observations $\boldsymbol{y}_i$ are assimilated in the 4D-VAR system at time i. The classic Bayesian approach determines the a posteriori solution $\hat{\boldsymbol{x}}$ (Rodgers, 2000):

$$\hat{\boldsymbol{x}} = \boldsymbol{x}_b + \mathbf{K}(\mathbf{H}\boldsymbol{x}-\boldsymbol{y}), \tag{3}$$

with $\mathbf{K}=\mathbf{B}\mathbf{H}^{\mathrm{T}}\left(\mathbf{H}\mathbf{B}\mathbf{H}^{\mathrm{T}}+\mathbf{R}\right)^{-1}$ and $\mathbf{H}$ is the Jacobian matrix corresponding to the CTM H (Arellano et al., 2004). The a posteriori error covariance matrix $\mathbf{A}$ can be written as

$$\mathbf{A} = \left(\mathbf{H}^{\mathrm{T}}\mathbf{R}^{-1}\mathbf{H}+\mathbf{B}^{-1}\right)^{-1}. \tag{4}$$

ACPD
11, 341–386, 2011

When the number of state vector variables is large, it is not possible to compute the inverse matrices in the above equations directly. Hence an iterative minimization algorithm is required. The conjugate gradient method (Fisher, 1998) can be used to minimize the cost function (2) if the CTM is linear. In general, the CTM H is nonlinear with respect to the state vector $\boldsymbol{x}$ since the CO emissions perturb OH concentrations and hence the CO sink term. However, for tropospheric CO, Pétron et al. (2002) have shown that to a reasonable approximation, the system can be linearized by using fixed OH fields. In this case the cost function $\mathcal{J}$ is quadratic and can be minimized using the conjugate gradient method (Fisher, 1998). This method is a generalization of the steepest descend method that also yields the leading eigenvalues λ_i and eigenvectors v_i of the Hessian of the cost function. The a posteriori error covariance matrix (Eq. 4) describing the uncertainty in the optimized state vector $\hat{\boldsymbol{x}}$, equals the inverse Hessian of the cost function. Hence, the a posteriori error covariance matrix is approximated by a finite combination of the leading eigenvalues and eigenvectors of the Hessian of the cost function added by the a priori error covariance matrix **B** (Fisher and Courtier, 1995):

$$\mathbf{A} \approx \mathbf{B} + \sum_{i=1}^{N} \left(\frac{1}{\lambda_i} - 1 \right) (\mathbf{L}v_i)(\mathbf{L}v_i)^{\mathrm{T}}, \tag{5}$$

where **L** is the preconditioner explained below.

The rate of convergence of the minimization is in general quite slow, but a preconditioner can be used to speed up the convergence rate. Fisher and Courtier (1995) have shown that the matrix **L** such that $\mathbf{L}\mathbf{L}^{\mathrm{T}}=\mathbf{B}$ is a suitable preconditioner when used in this 4D-VAR approach. However, due to the large number of state vector elements, it is not possible to store this preconditioner in this form in memory. We will follow the approach of Meirink et al. (2008b) to store the preconditioner **L**. In our study, we consider the method converged when the norm of the gradient of the cost function is reduced by 99%.

ACPD
11, 341–386, 2011

The chemical transport model H, the prior state $\boldsymbol{x}_b$ with uncertainty **B** and the observations $\boldsymbol{y}$ with their uncertainty **R** will be described in more detail in the following sections.

2.1 The chemical transport model TM5

The CTM (also called the forward model) used in this study to relate CO emissions to atmospheric CO mixing ratios is the two-way nested chemical transport model TM5 (Krol et al., 2005). TM5 is an offline model driven by 3-hourly meteorological fields (6-hourly for 3-D input fields) from the European Centre for Medium-Range Weather Forecasts (ECMWF). Here we do not use the full-chemistry TM5 model, but the so-called TM5 CO-only model (svn-version 3197). This model, running on a coarse $6^{\circ}\times4^{\circ}$ horizontal grid with 25 vertical layers in this study, deviates from the full chemistry version by employing simplified CO-OH chemistry. In order to keep the model linear, a monthly OH climatology is used (Spivakovsky et al., 2000), which is scaled by a factor 0.92 based on methyl chloroform simulations performed for 2000–2006 (Huijnen et al., 2010).

2.2 Specification of a priori state

The state vector ($\boldsymbol{x}$ in Eq. 2) consists of the variables to be optimized by the inversion. Here we distinguish between monthly surface CO emissions, monthly varying parameters that scale the chemical production of CO from oxidation of methane and NMVOCs, and the initial 3-D CO mixing ratio field. The emissions are divided in three categories: anthropogenic (combustion of fossil fuels and biofuels), natural sources (direct CO emissions from vegetation and the oceans) and biomass burning (open vegetation fires, both natural and human induced).

The a priori anthropogenic emissions are taken from the Emission Database for Global Atmospheric Research (EDGARv3.2) inventory (Olivier et al., 2000, 2003). The distribution of natural CO emissions (Houweling et al., 1998) is scaled to emit

ACPD
11, 341–386, 2011

115 Tg CO yr^{-1} which is well within the range of the estimate by Schade and Crutzen (1999) (50–170 Tg CO yr^{-1}). Biomass burning emissions are taken from GFED2 (van der Werf et al., 2006). Biomass burning CO is distributed over the vertical model grid as follows: 20% is released in the layers 0–100 m, 100–500 m and 500–1000 m. The remaining 40% is released between 1000–2000 m in accordance to Labonne et al. (2007). The sensitivity of the optimized emissions with respect to the chosen injection height is discussed further in Sect. 5.

The chemical production of CO from oxidation of methane and NMVOCs requires monthly 3-D CO production fields. Constant methane mixing ratios of 1800 parts per billion (ppb) are used throughout the atmosphere. Methane is oxidized by the OH climatology using a temperature dependent reaction rate constant (Seinfeld and Pandis, 2006)

$$k = 2.45 \cdot 10^{-12} \exp(-1775/T). \quad (6)$$

The CH_4 to CO conversion yield is taken as unity. We acknowledge the possibility of introducing a bias due to a significant N-S gradient in tropospheric CH_4 and a vertical gradient in stratospheric CH_4. The observed 10% N-S gradient in tropospheric methane would result in a 10% gradient in CO produced from methane oxidation. Since in our approach, about 875 Tg CO is produced annually from CH_4 oxidation, this leads to an overestimate of 45 Tg CO yr^{-1} on the SH and a similar underestimate on the NH. Although such a bias is small compared to the global CO emissions and chemical production, we will improve the CH_4 oxidation scheme in the next version of the 4D-VAR system.

A full-chemistry model run using TM4 (Myriokefalitakis et al., 2008) yields monthly 3-D CO fields produced by oxidation of biogenic and anthropogenic hydrocarbons. We construct the monthly NMVOC-CO source by subtracting the monthly CH_4-CO described above from the total fields. The total prior CO source from methane and NMVOCs is scaled to 1600 Tg CO yr^{-1} within the range of values used in the literature (1279–1644 Tg CO yr^{-1}) (e.g., Kopacz et al., 2010; Duncan et al., 2007; Bergamaschi

ACPD
11, 341–386, 2011

et al., 2000; Müller and Stavrakou, 2005). The CH_4-CO and NMVOC-CO fields themselves will not be optimized: instead a monthly scaling factor with unit a priori value is optimized. Hence, for these sources we apply a traditional synthesis inversion in the sense that the prior spatial emission patterns are constant and only the global total magnitude of CH_4-CO and NMVOC-CO is optimized.

A forward model simulation with these a priori emissions has been performed for the years 2002–2005 and daily mean CO mixing ratios have been archived. The a priori initial CO mixing ratio field is taken from this archive and further optimized by including the initial 3-D field in the state vector (Meirink et al., 2008b).

2.3 Specification of a priori uncertainties

2.3.1 Emissions

The prior emission errors on grid-scale are set in such a way that in combination with prior correlations (see below), the prior emission errors aggregated to continental regions are in a realistic range. The prior anthropogenic emission inventory used in this study (EDGAR v3.2) is compiled for the year 1995. Inverting for the years 2003/2004, we expect large emission increments due to rapid economic development, particularly in Asia. Hence we assign large errors to this region. In contrast, for the Western developed world (North America, Europe and Australia) we expect that the 2003/2004 anthropogenic emissions are close or somewhat smaller compared to 1995. Therefore, we apply grid-scale errors of 250% of the corresponding grid-scale emission for the developing world (Asia, Africa and South America) and 50% for the Western developed world. With these settings, realistic continental-scale errors are computed for the developing world (58–72%) and the Western developed world (20–48%).

The grid-scale prior emission errors for biomass burning and the natural source are set to 250% of the corresponding grid-scale emission, since both inventories bear large uncertainties. For both sources this leads to prior continental emission errors in the range of 40–100%.

ACPD
11, 341–386, 2011

Emission uncertainties are correlated in time and space resulting in a reduction of the effective number of variables to be optimized. For the three emission categories we use a Gaussian spatial correlation length of 1000 km. An e-folding temporal correlation length of 9.5 months (0.9 month to month correlation) is chosen for anthropogenic emissions because we do not expect pronounced seasonal cycles for this emission category. Due to the variable nature of fires in time, the temporal correlation length for biomass burning emissions is set to 0.62 months (0.2 month to month correlation). For natural emissions the temporal correlation length is set to 9.5 months.

2.3.2 Initial concentration field and additional parameters

The grid-scale prior initial concentration error is 5% of the corresponding prior initial concentration. The initial concentration field is correlated in space by a Gaussian correlation length of 1000 km as in Meirink et al. (2008b). The a priori errors on the monthly scaling factors for CO production from methane and NMVOCs are set to 2% and 8%, respectively. The scaling factors are correlated in time with a correlation length of 3 months (0.7 month to month correlation). This tight error setting is chosen because the posterior emission estimates are quite sensitive to the combination of anthropogenic and NMVOC prior emission uncertainties as discussed further in Sect. 5.

2.4 Atmospheric observations

In this first TM5 CO inversion study, only surface observations from NOAA/ESRL GMD are assimilated in the 4D-VAR system. The NOAA surface network provides CO observations from a globally distributed network of stations (Novelli et al., 1998, 2003). A subset of 31 stations, mainly remote stations and stations at larger distances from continental source regions are used in the inversions. Stations close to source regions as well as other stations for which we expect large model errors due to the coarse model resolution are left out. The selected stations are shown in Fig. 1. The observation error consists of the measurement error and the model error. The measurement

ACPD
11, 341–386, 2011

error is set to 1.5 ppb. The model error in the vertical direction is based on the modeled CO mixing ratio gradient for the grid boxes adjacent to the one the station is in (Bergamaschi et al., 2005). For the horizontal model error, subgrid-scale variability of the emissions is accounted for as described in Bergamaschi et al. (2010). The model error is usually much larger than the measurement error for stations on the NH. Only in remote areas in the SH, the measurement error is the dominant term in the observational error. No correlations between the observations are set resulting in a diagonal observational error covariance matrix **R**.

2.5 Inversion specifics

In this study the simulations with TM5 are performed on a rather coarse 6°×4° horizontal grid with 25 vertical layers. This means that after the application of emissions each time step, the CO mixing ratio is smeared out over the entire grid box. Hence, we do not expect the model to simulate all measured pollution events at non-background stations. To account for this and to prevent possible biases due to a few single outliers, the inversion is done in two cycles: After the first inversion we reject all data points that are outside a 3σ error range of the model simulation (Bergamaschi et al., 2010). Then the second inversion cycle is performed. In the CH_4 inversion of Bergamaschi et al. (2010), typically 3% of the data were rejected, but the a posteriori emissions for both inversion cycles did not differ very much in general. However, in the current study, focusing on the shorter-lived CO, approximately 15–20% of the data from the first inversion are rejected. Inferred continental emissions in the second cycle are within 15% of the emissions in the first cycle for most sources/regions and show a similar pattern of adjustments. However, biomass burning emissions for Africa and Asia may differ up to 30%. This is due to the low month to month correlation of biomass burning emissions and the sparsity of NOAA surface observations in these regions.

A sensitivity study with doubled observational errors reduced the number of rejected data points to 7%. However, larger observational errors result in a less constrained system and inferred emission estimates remain closer to the prior compared to an

ACPD
11, 341–386, 2011

inversion with more strict observational errors. This is illustrated by the behaviour of the cost function. The background part of the optimized cost function (first term in Eq. 2) amounts to 238 compared to 460 in the base inversion (presented in Sect. 3). The observational part of the cost function (second term in Eq. 2) amounts to 839 compared to 1139 in the base inversion, again due to the larger observational errors.

The years 2003 and 2004 are inverted separately because the inversions are computer-time demanding. The inversions use a one month spin up, in which the emissions are optimized already, but not analyzed, and 2 months spin down to supply enough observations to optimize the emissions in the last months of the year. Given a lifetime of about 2 months for CO, it has been investigated that to optimize emissions in a certain month m, it is sufficient to use observations for months m, m+1 and m+2 (not shown). Observations at later times will not significantly influence the emissions in month m, because the emission signal is sufficiently diluted and chemically removed by that time. It should be borne in mind, however, that emissions in month m are still influenced by emission estimates in surrounding months (m–3,...,m+3) via the prior temporal correlation length.

The length of the state vector is 189030, according to (15 months×3 source categories+25 vertical layers of the initial concentration field)×(60×45 grid boxes)+ 15 months×2 scaling factors. In contrast, the total number of observations is only about 1400 per year. By introducing a non-diagonal prior error covariance matrix, the number of "true" unknowns is greatly reduced to approximately 25 000, but the problem still remains underdetermined (data sparse and hence strongly dependent on a priori knowledge of the emissions). Nevertheless, a grid-scale inversion is performed here to reduce the risk of aggregation errors, which often occur in a big region approach (Meirink et al., 2008b; Stavrakou and Müller, 2006) and to prepare for the future ingestion of large amounts of satellite data.

ACPD
11, 341–386, 2011

3 Inversion results

3.1 Comparison of modeled and observed CO mixing ratios

In this section we will discuss the capability of the current 4D-VAR system to adjust the state vector in such a way that background CO mixing ratios as well as observed large scale pollution events are adequately captured. Figure 2 shows the prior and posterior simulation of CO mixing ratios and surface observations for a subset of four stations used in the inversion (purple squares in Fig. 1). All panels show that the model simulation with a priori settings (yellow) is capable to simulate the seasonal cycle and some pollution peaks even though the simulations are performed on a coarse $6^{\circ}\times4^{\circ}$ grid. However, differences with the observations (red) up to 50 ppb are observed. In contrast, the posterior simulation (blue) fits the observations at all four stations rather well. This better fit is obviously caused by combined changes in the surface emissions and in the global source of CO from methane and NMVOCs. A quantitative analysis for all assimilated stations is shown in Table 1 for 2004. Here we present the bias per station for the prior and posterior simulation of the two inversion cycles. A value for the goodness of fit parameter χ^2/n is also given in this table. A χ^2/n value close to 1 indicates that the system is behaving well.

For station Cold Bay, Alaska (Fig. 2a), representing the high latitude NH, the prior simulation underestimates observed CO mixing ratios up to 50 ppb, in the period September 2003 to February 2004 and from September 2004 to January 2005. For the year 2003, the inversion decreases biomass burning emissions from Russia in spring, but emissions are increased in summer. The posterior annual biomass burning emission estimate for Russia in 2003 is 97±28 Tg CO (compared to the prior estimate of 75±77 Tg CO), well within the range reported by Kasischke et al. (2005) (55–139 Tg CO yr^{-1}). This shows that Russian fires account for 60% of the total CO emissions from biomass burning in Asia in 2003 (158 Tg CO, Table 2). In contrast, in 2004 the inversion increases the Alaskan and Canadian biomass burning emissions in summer, from a prior emission estimate of 16±19 Tg CO from June to August to

ACPD
11, 341–386, 2011

36±9 Tg CO as posterior emission estimate. This increase in Alaskan and Canadian biomass burning emissions was also reported by Pfister et al. (2005) and Turquety et al. (2007), and in closer correspondence to 30 Tg CO as estimated in the recently released updated GFED (version 3.1, van der Werf et al., 2010). Pfister et al. (2005) inferred CO emissions using satellite observations and reported a posterior emission estimate of 30±5 Tg CO. Turquety et al. (2007) constructed a daily biomass burning emission inventory taking into account the emissions from peat burning. They estimated a total of 30 Tg CO from June to August 2004 for North America. Outside the biomass burning season, the inversion attributes increased CO levels to enhanced anthropogenic emissions in East Asia. From Table 1 it is observed that for station Cold Bay the prior bias decreases from −9.7 ppb in the first inversion cycle to −4.3 ppb in the second inversion cycle due to rejection of observations that are not reproduced by the model. This rejection improves the a posteriori χ^2/n diagnostic for this station from 2.7 to 1.15. The posterior bias is reduced to nearly zero.

For station Sand Island, Midway (Fig. 2b), the prior simulation underestimates observations during the entire period. This was expected due to the use of the EDGARv3.2 inventory (compiled for the year 1995) for anthropogenic emissions for this region for the years 2003 and 2004. Rapid economic development, particularly in China and India over the last decade led to increased anthropogenic emissions. The posterior simulation shows that increased anthropogenic emissions over China and India (the inversion roughly doubles Asian anthropogenic emissions, see Table 2) results in 15–25 ppb higher CO mixing ratios on stations downwind of South East Asia. Individual observations due to pollution plumes that were not reproduced in the prior simulation are captured better by the model in the posterior simulation. This is due to the fact that the 4D-VAR system computes emission increments on the grid-scale of the underlying chemistry-transport model and hence, has the ability to better exploit the spatial information present in the measurements. It is acknowledged, however, that a higher spatial resolution is required to reduce the artificial smearing of concentration gradients.

ACPD
11, 341–386, 2011

The tropics are represented here by station Ascension Island (Fig. 2c), and although the improvement from prior to posterior simulation is not clearly visible, Table 1 shows that the posterior bias is nearly zero, and the χ^2/n diagnostic is reduced from 3.03 to 1.22. For the remote SH, represented here by station South Pole (Fig. 2d), the prior simulation overestimates the observations by 5–10 ppb all year long. The inversion attributes this to too high production of CO from NMVOCs since the station is far away from major sources, but neglecting the N-S gradient in tropospheric methane in the model, as discussed before, may also play a role. Again, the posterior bias is nearly zero in both inversion cycles and the χ^2/n diagnostic obtains a value of 1.01.

Table 1 shows that the inversion reduces prior biases for most of the stations and that the χ^2/n diagnostic is decreased to approximately 1. However, for remote stations in the SH, χ^2/n shows values far smaller than 1 indicating that the measurement error of 1.5 ppb might be too conservative or indicating the need to take correlations in the observation errors into account.

3.2 Posterior emission estimates

We present the posterior emission estimates and their uncertainties aggregated over continental scale regions as yearly totals, because the monthly emission estimates on grid-scale level are highly variable as a consequence of the loose prior error settings and the small amount of observations. Also, as shown by Meirink et al. (2008b), the posterior errors converge only rapidly for larger spatial and temporal scales (Fig. 3).

Table 2 and Fig. 3 (blue, solid line) show that on a global scale, a substantial uncertainty reduction of 60% for the anthropogenic emissions is achieved. Columns 2 and 3 of Table 2 show that in particular Asian anthropogenic emissions are well constrained by the observations (258±150 Tg CO a priori compared to 497±82 Tg CO in 2003 and 526±75 Tg CO in 2004 a posteriori, see also Fig. 3, dotted blue line). In contrast, African and South American anthropogenic emissions show a negligible uncertainty reduction (Fig. 3, dash-dotted and dashed line, respectively). This was expected though, since atmospheric observations mainly constrain the total emissions and the

ACPD
11, 341–386, 2011

error reduction in those regions is largest for the dominant biomass burning source term.

For biomass burning emissions, uncertainty reduction is achieved in South America (e.g., 98±105 Tg CO a priori compared to 136±39 Tg CO a posteriori in 2004, Fig. 3 red dashed line), Asia (e.g., 114±81 Tg CO a priori compared to 158±38 Tg CO in 2003 (not shown)) and North America (23±19 Tg CO a priori and 47±10 Tg CO a posteriori in 2004 only). Large changes in biomass burning emissions from 2003 to 2004 are observed for South America and Africa. For South America (with posterior emissions of 75±37 Tg CO in 2003 and 136±39 Tg CO in 2004) this increment was partly present in the GFED2 prior. Higher emissions in 2004 were also confirmed by observations from the Scanning Imaging Absorption Spectrometer for Atmospheric Cartography (SCIAMACHY) (Gloudemans et al., 2009) showing the large inter annual variability in South American biomass burning emissions. In contrast, the posterior biomass burning emission estimates for Africa in 2003 and 2004 seem to compensate for the difference in NMVOC-CO. This is confirmed by the relatively small error reduction and by the study of Chevallier et al. (2009), who optimized African emissions using MOPITT observations for 2000 to 2006 and did not show large inter annual variability from 2003 to 2004. Table 2 (columns 6 and 7) shows that natural emissions are hardly constrained by the data.

Finally, the uncertainty of the global scaling parameters for the production of CO from methane and NMVOC oxidation is only slightly reduced from the prior to the posterior estimate. This indicates that the current observational dataset does not constrain these parameters substantially. However, the value of the scaling factor for the NMVOC-CO (CO from NMVOCs) source is adjusted significantly from a prior global total of 812±40 Tg CO to a posterior global total of 574±38 Tg CO in 2003 and 410±36 Tg CO in 2004. Despite the small prior error, the NMVOC-CO emissions are considerably reduced, far outside the 2σ (95%) interval, which is mainly due to the overall very small weight of the single monthly NMVOC-CO scaling parameters in the cost function. Small error settings appeared to be necessary, because the a priori error settings of this

ACPD
11, 341–386, 2011

global parameter have a strong influence on the solution of the inversion. Sensitivity studies with respect to these error settings have been performed as discussed in more detail in Sect. 5.

3.3 Validation with independent NOAA aircraft observations and MOPITT total columns

We validate our inferred emissions with independent (that is, non-assimilated) aircraft observations from the NOAA aircraft program for 2004. The comparison with aircraft data provides a valuable test for the vertical transport in the model. The NOAA profiles are taken mainly over North America. Figure 4 shows monthly mean deviations (model-observations) for the prior and posterior simulation for aircraft samples with altitudes above 2000 m, thus representing the free troposphere. The prior simulation underestimates the observations throughout the year (except for May and June) probably due to too low anthropogenic emissions in East Asia. The significant overestimation of the prior simulation in May and June is attributed to a too large a priori source of CO from NMVOCs. The posterior simulation matches the observations much better, since the inversion increased Asian anthropogenic emissions and reduced the NMVOC-CO source (Table 2), in particular in May and June (not shown). The uncertainty, given here as a 1σ deviation from the mean, is not reduced significantly from prior to posterior simulation because these observations are not assimilated. Overall, the mean monthly difference is reduced by 50–90% except for April when deviations were small anyway. The annual mean and standard deviation of the residuals is -6.4 ± 23 ppb a priori and -0.5 ± 22 ppb a posteriori, showing that the inversion is capable to improve the comparison with independent observations in the free troposphere.

We further validate our posterior emissions with CO total column retrievals from MOPITT V4 (level 3, gridded daily profiles, Deeter et al., 2003, 2007, 2010). The MOPITT instrument is mainly sensitive to free tropospheric CO (4–7 km altitude) and CO at this altitude originates from oxidation of methane or convective transport of surface CO. Figure 5 shows a comparison of observed and modeled CO total columns, where

ACPD
11, 341–386, 2011

the MOPITT averaging kernels are used to compare properly. Surprisingly, the overall agreement with MOPITT seems to deteriorate from the prior to the posterior simulation. However, over the well-constrained NH, the agreement improves slightly for 2004 from a prior underestimate of 12% to a posterior overestimate of 6%. Over the continents, the agreement improves even more. For 2003, the prior simulation underestimates MOPITT by 8% but the posterior simulation overestimates MOPITT by 13%. In the remote SH (30° to 62° S), the comparison with MOPITT deteriorates from a slight model underestimate of 6% a priori to an underestimate of 40% a posteriori in both years. The prior simulation overestimates surface observations of CO at the remote SH stations (see Fig. 2d). These SH surface observations thus cause a decrease in CO sources (mainly NMVOC-CO) which results in even less CO compared to MOPITT. The underestimation of the model may have to do with the vertical transport in the model. For instance, if vertical transport in the model is too slow, CO emissions will remain at low altitudes where the MOPITT instrument is not very sensitive. The comparison with NOAA aircraft profiles showed however that the vertical transport in TM5 is reasonable. Hence, a possible bias in the MOPITT V4 product as was the case for the previous product MOPITT V3 (Emmons et al., 2009; de Laat et al., 2010) may also play a role. The suspect land-sea differences in Fig. 5, especially in the vicinity of desert regions indeed indicate that not all retrieval issues may have yet been resolved.

In conclusion, validating our inversion results with independent aircraft data shows an improved agreement with respect to the prior simulation in the free troposphere even though only surface observations are assimilated. For satellite data, the agreement with MOPITT total column CO shows a slight improvement over the well-constrained NH, but deteriorates in the SH below 30° S.

3.4 Comparison with recent inverse modeling results

The posterior emissions match other recent inverse modeling results quite well as shown in Table 3. Pison et al. (2009) inverted emissions of CO, methane and H_2 simultaneously, using observations from NOAA and updated the OH field within the

ACPD
11, 341–386, 2011

optimization by assimilating methyl chloroform observations. Results are comparable to our results, but slightly higher for Europe and lower for South America. However, the Australian source of Pison et al. (2009) included CO emissions from Indonesia and is thus significantly higher than the current study. Kopacz et al. (2010) used satellite data (from MOPITT, the Atmospheric Infrared Sounder (AIRS) instrument and SCIAMACHY) to optimize CO emissions for the period May 2004 to April 2005 and their results showed slightly higher emissions over South America and Asia, but significantly lower emissions over North America. This might be due to their very low prior value for anthropogenic emissions over the United States (35 Tg CO) based on the US Environmental Protection Agency National Emission Inventory for 1999 (EPA_NEI99). This value was decreased by 60% following Hudman et al. (2008). In this study we use 105 Tg CO as prior anthropogenic emission over North America. Jones et al. (2009) optimized emissions for November 2004 only using observations from the MOPITT and TES instruments, but they presented their results as yearly totals. These results are also comparable to the current study except for the Australian source. This is explained by their inclusion of Indonesia into this region. Chevallier et al. (2009) have performed a detailed analysis of African CO emissions for the period 2000–2006. The total emissions are 25% lower than in this study but stay well within the error bounds. The difference with our results is probably explained by the lack of surface data in the tropics. Chevallier et al. (2009) used MOPITT data to constrain the CO emissions and anthropogenic emissions in particular were more constrained than in the current study. Finally, the large increment in Asian anthropogenic emissions shown in Table 2 also confirms the previous findings of e.g., Kasibhatla et al. (2002) and Arellano et al. (2004) that anthropogenic emissions over Asia are too low in EDGARv3.2. All inversions roughly doubled the Asian emission estimate.

ACPD
11, 341–386, 2011

4 Discussion

In our inversions we have used a limited amount of observations from the NOAA surface network. A consequence of solving a data sparse system is a large solution space, because not all degrees of freedom (≈25 000) are constrained by the observations (≈1400 per year). Thus, the obtained solution will depend on the prior emissions and their error settings. Another consequence might be that model errors are compensated for by emission increments. To investigate these issues, a series of sensitivity studies is presented in Sect. 5.

The 4D-VAR system is in general not capable to distinguish between the anthropogenic, biomass burning and the NMVOC-CO sources. Although globally the posterior source estimate for these three sources is 1744±76 Tg CO in 2003 and 1690±75 Tg CO in 2004 and the difference is well within the error bounds, in particular anthropogenic emissions and the NMVOC-CO source show large shifts from 2003 to 2004. Some of these shifts seem not driven by observations, but rather a compensation for a change in another source. For example, the derived NMVOC-CO source shows a large drop from 2003 to 2004 (574 Tg CO in 2003 to 410 Tg CO in 2004), which seems to be an artefact of the system rather than a real signal of reduced NMVOC-CO, caused by the design of the system. Since the global NMVOC-CO source is scaled by a monthly varying parameter, the large changes in these parameters have only little effect on the background part of the cost function (Eq. 2 left-hand term), but a huge effect on the observational part of the cost function (Eq. 2 right-hand term) in particular in the SH. This drop is compensated (within the error bounds) by increased anthropogenic emissions (770 Tg CO in 2003 to 871 Tg CO in 2004). We calculated the posterior correlation (from the posterior covariance matrix A, Eq. 2) between the two sources to be negative (−0.29 in 2003 and −0.23 in 2004), further indicating this compensation mechanism. The estimate for biomass burning seems to be more robust on a global scale (400 Tg CO in 2003 versus 409 Tg CO in 2004), but we observe large differences on continental scales between the two years. For example, North American biomass

ACPD
11, 341–386, 2011

burning emissions in 2003 increase without a reduction in the error from 32±32 Tg CO to 61±30 Tg CO (Table 2). Hence, the increase seems a further compensation for the reduction in the NMVOC-CO source.

For specific regions where biomass burning emissions are the dominant source (e.g., South America), the 4D-VAR system appears to be capable to distinguish biomass burning emissions from the anthropogenic source. This is probably caused by the timing of these emissions as proposed by the prior inventory and the low month to month temporal correlation used. An example of this differentiation between anthropogenic and biomass burning sources is observed for North America and South America in 2004. Although anthropogenic source estimates show no uncertainty reduction and are equal or slightly smaller than the prior estimate, biomass burning emissions increase from the prior emission estimate and the posterior emission uncertainty is reduced significantly. In 2003 this is also observed in South America, where anthropogenic emissions are even reduced to non-significant negative values (Table 2), while biomass burning emissions increase from 60±48 to 75±37 Tg CO yr^{-1}.

5 Sensitivity analysis

In this section we discuss 7 sensitivity studies with respect to prior settings and model errors. Sensitivity studies S1–S4 focus on the effect of the prior grid-scale error for the surface emissions and the prior NMVOC-CO error on the derived posterior emissions. Study GFED3.1 uses the new version of the GFED product (GFEDv3.1, van der Werf et al., 2010). For the year 2004, this biomass burning inventory prescribes lower emissions by a factor 2 to 3 from January to March compared to GFED2. Peak emissions in September in GFED2 of 69 Tg CO/month globally are reduced to 55 Tg CO/month in GFED3.1.

Since the distribution of OH and its north-south gradient remains uncertain, we also investigate the influence of the tropospheric OH distribution on the inferred emissions by using an OH field computed from a full-chemistry simulation with TM5 (Huijnen et al.,

ACPD
11, 341–386, 2011

2010) and scaled by a factor 1.02 to obtain comparable CO and methyl chloroform lifetimes as for the OH field used in the base inversion. Compared to the OH field of the base inversion, the north-south gradient (computed as an airmass-weighted average (Lawrence et al., 2001)) in the TM5-OH field is more pronounced (NH/SH ratio of 1.15) compared to the OH field used in the base inversion (NH/SH ratio of 1.0).

Study FVERT focusses on model uncertainty in the vertical distribution of biomass burning emissions. The base inversion uses an injection height for biomass burning emissions up to 2000 m (distributed as 20% in layers 0–100 m, 100–500 m and 500–1000 m and 40% in 1000–2000 m layer). However, some recent studies (Gonzi and Palmer, 2010; Val Martin et al., 2009) found evidence that biomass burning emissions are partly injected higher up in the atmosphere. In study FVERT we apply a vertical distribution of biomass burning emissions following the results of Gonzi and Palmer (2010). The vertical biomass burning emission distribution is defined as

- Boreal region (>30° N): 82% below 2 km, 10% in 2–5 km, 2.5% in each of the layers 5–8 km and 8–11 km. The remaining 3% is injected above 11 km.
- Tropical region: 85% below 2 km, 10% in 2–5 km, 2.5% in both layers 5–8 km and 8–11 km.

A summary of the sensitivity studies is provided in Table 4. The inversion results for these sensitivity tests are averaged globally for 2004 and are summarized in Table 5, where we omit the natural emissions and CH_4-CO since these sources do not change significantly from the prior to the posterior emission estimates in the base inversion.

5.1 Sensitivity studies S1–S4

Overall, the inferred anthropogenic and biomass burning emissions for studies S1 to S4 (Table 5) are quite robust as nearly all posterior emission estimates are within the error bounds of each other. The differences in emission estimates for S1 to S4 are likely caused by the incapability of the system to separate the anthropogenic and NMVOC-CO sources. This results in a compensation of one source for another as discussed

ACPD
11, 341–386, 2011

before. This compensation mechanism depends on the combination of the prior errors in the anthropogenic and NMVOC-CO emissions. For example, in sensitivity study S1, the NMVOC-CO prior error dominates, resulting in less reduction in this source compared to the base inversion. The anthropogenic source compensates for this by reducing the emission estimate with 67 Tg CO yr^{-1} compared to the base inversion. In contrast, for sensitivity study S3, the anthropogenic emission prior error dominates, resulting in higher anthropogenic emissions and a more pronounced reduction in the NMVOC-CO source compared to the base inversion. Biomass burning emission estimates are only slightly sensitive to the prior error settings, as all sensitivity studies estimate posterior biomass burning emissions in the range 400–477 Tg CO yr^{-1}.

We conclude that anthropogenic emissions and the NMVOC-CO source can not be properly separated by assimilation of a limited number of observations. The situation will likely improve when we start the assimilation of large amounts of satellite data in our system. However, a separation between different source categories will remain extremely challenging and might require additional information from other sources. For example, satellite observations of formaldehyde and glyoxal may further constrain the distribution of NMVOCs (Stavrakou et al., 2009).

5.2 Sensitivity study GFED3.1

The results for sensitivity study GFED3.1 (Table 5) show an increase in biomass burning of 30 Tg CO yr^{-1} with respect to the prior estimate of 334 Tg CO yr^{-1}. Biomass burning emissions mainly increase in South America (+45 Tg CO yr^{-1}) and Africa (+9 Tg CO yr^{-1}). However, Asian biomass burning emissions decrease by 32 Tg CO yr^{-1}. This behavior was also observed for the base inversion. For example, for the base inversion the increase in South America was 38 Tg CO, whereas for Africa there was no significant increase. Asian biomass burning emissions decreased by 56 Tg CO. This sensitivity study does not support the decrease in global emissions in GFED3.1 compared to GFED2, although regionally results improved (e.g., North America and Asia). This could be partly due to the underestimation of agricultural

ACPD
11, 341–386, 2011

waste burning and deforestation fires (van der Werf et al., 2010). To compensate for the lower biomass burning emissions, anthropogenic emissions (932±73 Tg CO) and the NMVOC-CO source (433 Tg CO) are increased with respect to the base inversion.

5.3 Sensitivity study OH

The OH field from the TM5 full-chemistry simulation shows lower OH over tropical land masses compared to the OH field from Spivakovsky et al. (2000) (Fig. 6, top), in particular over South America. This OH gap is present since large amounts of emitted isoprene are oxidized by OH and hence reduce OH concentrations in the model. However, as shown by Lelieveld et al. (2008), this OH gap is not confirmed by field campaigns that show high OH over the tropical forests. An OH recycling mechanism was proposed by Lelieveld et al. (2008), but was not yet incorporated in the TM5 simulation (Huijnen et al., 2010). Lower OH concentrations over tropical land masses (Fig. 6, top) result in a reduction of biomass burning emissions of 88 Tg CO yr^{-1} globally in 2004 compared to the base inversion (Table 5, Fig. 6 bottom). Africa (−51 Tg CO yr^{-1}) and South America (−30 Tg CO yr^{-1}) contribute substantially to this decrease. The NMVOC-CO source is reduced to 369 Tg CO yr^{-1}, which is 41 Tg CO yr^{-1} lower than in the base inversion. This reduction is also attributed to the lower OH concentrations in the SH. In contrast, the NH OH concentration is higher compared to the OH field from Spivakovsky et al. (2000). Therefore, higher global anthropogenic emissions are observed for this study (967 Tg CO yr^{-1}) compared to the base inversion (871 Tg CO yr^{-1}). This difference is clearly observed over India in Fig. 6. The comparison with MOPITT is not improved with respect to the base inversion (not shown): The remote SH still shows an underestimate of MOPITT total columns.

5.4 Sensitivity study FVERT

When biomass burning CO emissions are released higher up in the atmosphere, one would expect to infer higher biomass burning emissions, since the surface concen-

ACPD
11, 341–386, 2011

trations of biomass burning CO decrease and thus, higher CO surface emissions are required to match the observations. Indeed, it is observed that the global biomass burning emissions increase with 75 Tg CO yr^{-1} with respect to the base inversion (Table 5). Moreover, this increase is only partly compensated for by decreased anthropogenic emissions (−21 Tg CO yr^{-1}) and a decrease in the NMVOC-CO source (−7 Tg CO yr^{-1}), indicating that a part of the biomass burning CO emissions is not detected by the surface network. Higher biomass burning CO emissions with respect to the base inversion cause the comparison with MOPITT CO total columns to change: Over the main biomass burning regions in Africa, South America and South East Asia, the comparison deteriorates, because the base inversion already overestimates MOPITT CO total columns over these regions (Fig. 5d). On the remote SH, the comparison does not change significantly since the NMVOC-CO source shows only minor changes with respect to the base inversion. We conclude that the biomass burning injection height is a potentially important parameter to take into account in inversions. However, the agreement with MOPITT CO on the SH total columns does not improve, mainly because it seems that the surface observations and MOPITT CO total columns are not consistent in the model. This was also observed by Kopacz et al. (2010). They inverted CO emissions using satellite data only and SH stations used as validation showed a poorer agreement in the posterior simulation compared to the prior.

The planned assimilation of MOPITT CO total columns may result in a less pronounced reduction in the NMVOC-CO in order to fit the satellite data. In turn, more NMVOC-CO may result in lower biomass burning emissions and hence, an improved agreement over the main biomass burning regions in the SH. Moreover, biomass burning emissions might become more comparable with the new GFED3.1 (van der Werf et al., 2010) product. However, when assimilating both MOPITT CO total column data and surface network observations in the TM5 model, the system will try to find a compromise between both data streams. A bias correction for MOPITT profiles seems to be necessary to get a consistent picture of CO sources in TM5, particularly on the SH.

ACPD
11, 341–386, 2011

6 Conclusions

We have presented a 4D-VAR data assimilation system for CO using simplified chemistry and a fixed OH field, meant to assimilate large satellite datasets, but tested here using surface network observations from NOAA only. The proper functioning of the system is shown by the fact that the posterior simulation reproduces background CO mixing ratios including events with enhanced CO mixing ratios. The mean bias between modeled CO mixing ratios and observations from the NOAA surface network reduces for nearly all stations and the χ^2/n characteristic is reduced to values around 1, indicating that the chosen prior errors result in a well-balanced system. As expected, regions that are well constrained by the observational data show large uncertainty reductions, whereas non-constrained regions show only minor error reductions.

Our annual continental emissions compare well with recent inverse modeling studies, indicating that the global budget of CO is well constrained in our inversion. The posterior emissions have been validated using non-assimilated aircraft data from NOAA and vertical column data from MOPITT V4. The forward simulation with the inferred emissions showed much more resemblance with NOAA aircraft observations in the free troposphere compared to the prior simulation, showing that the inversion is capable to improve the free tropospheric CO distribution even though only surface observations are assimilated. The comparison with MOPITT total column CO improves slightly over the well-constrained NH from the prior to the posterior simulation. However, in the SH, the comparison with MOPITT deteriorates from approximately a 6% low a priori to a 40% low a posteriori, due to an emission decrease forced by SH surface observations.

With the limited amount of assimilated data and the low spatiotemporal resolution of surface network observations, it is difficult to distinguish between anthropogenic emissions and the NMVOC-CO source. Hence, emission increments in one source, to compensate for emission changes in another, are observed. The prior error settings for anthropogenic emissions and the NMVOC-CO source influence this compensation as

ACPD
11, 341–386, 2011

was confirmed by sensitivity studies. However, regions where the timing of the biomass burning emissions is very important (e.g., South America) show that it is possible to distinguish between anthropogenic and biomass burning emissions.

The impact of model errors on the inversion results was investigated by employing a different OH field and a different biomass burning emission height. An OH distribution from a full-chemistry simulation with TM5 with a more pronounced N-S ratio in OH largely influenced the inversion results: Biomass burning emissions and NMVOC-CO reduced whereas the anthropogenic emissions increased compared to the base inversion. This shows that the OH distribution over the NH and SH is critical for CO inversions. For this OH field the comparison with MOPITT total column CO in the SH did not improve and even less CO emissions were inferred on the SH. The sensitivity study with a different biomass burning injection height showed that the vertical distribution of biomass burning also largely influences the inversion results. Biomass burning emissions increased by 75 Tg CO yr^{-1} with respect to the base inversion. Again, the comparison with MOPITT total columns did not improve. Increased biomass burning emissions over emission hotspots in South America, Central Africa and Indonesia result in an even larger discrepancy with MOPITT total columns. On the remote SH the comparison with MOPITT was similarly poor as in the base inversion.

The use of satellite data in combination with the network of surface observations is an obvious next step. Assimilation of MOPITT total column CO is expected to lead to more NMVOC-CO on the remote SH, which in turn might reduce biomass burning emissions over the fire hotspots in the SH. Lower biomass burning emissions will be more in line with the new GFED3.1 product. However, surface and satellite observations over the remote SH may bring conflicting information. Therefore, like in the assimilation of SCIAMACHY methane observations (Bergamaschi et al., 2009) a bias correction scheme for satellite data seems necessary.

Acknowledgements. This research was supported by the Dutch User Support Programme 2006–2010 under project GO-AO/05. We also thank the MOPITT team for the MOPITT data. The Dutch National Computer Facility (NCF) is acknowledged for computer resources.

ACPD
11, 341–386, 2011

References

Arellano, Jr., A. F., Kasibhatla, P., Giglio, L., van der Werf, G., and Randerson, J.: Top-down estimates of global CO sources using MOPITT measurements, Geophys. Res. Lett., 31, L01104, doi:10.1029/2003GL018609, 2004. 345, 346, 360

Arellano, Jr., A. F., Kasibhatla, P., Giglio, L., van der Werf, G., Randerson, J., and Collatz, G.: Time-dependent inversion estimates of global biomass burning CO emissions using Measurement of Pollution in the Troposphere (MOPITT) measurements, J. Geophys. Res., 111, D09303, doi:10.1029/2005JD006613, 2006. 345

Bergamaschi, P., Hein, R., Heimann, M., and Crutzen, P. J.: Inverse modeling of the global CO cycle 1. Inversion of CO mixing ratios, J. Geophys. Res., 105, 1909–1927, 2000. 345, 349

Bergamaschi, P., Krol, M., Dentener, F., Vermeulen, A., Meinhardt, F., Graul, R., Ramonet, M., Peters, W., and Dlugokencky, E. J.: Inverse modelling of national and European CH_4 emissions using the atmospheric zoom model TM5, Atmos. Chem. Phys., 5, 2431–2460, doi:10.5194/acp-5-2431-2005, 2005. 352

Bergamaschi, P., Frankenberg, C., Meirink, J.-F., Krol, M., Villani, G., Houweling, S., Dentener, F., Dlugokencky, E. J., and Engel, A.: Inverse modeling of global and regional CH_4 emissions based on recently revised SCIAMACHY retrievals, J. Geophys. Res., 114, D22301, doi:10.1029/2009JD012287, 2009. 345, 346, 368

Bergamaschi, P., Krol, M., Meirink, J. F., Dentener, F., Segers, A., van Aardenne, J., Monni, S., Vermeulen, A., Schmidt, M., Ramonet, M., Yver, C., Meinhardt, F., Nisbet, E. G., Fisher, R., O'Doherty, S., and Dlugokencky, E. J.: Inverse modeling of European CH_4 emissions 2001–2006, J. Geophys. Res., 115, 4703–4715, 2010. 352

Chevallier, F., Fortems, A., Bousquet, P., Pison, I., Szopa, S., Devaux, M., and Hauglustaine, D. A.: African CO emissions between years 2000 and 2006 as estimated from MOPITT observations, Biogeosciences, 6, 103–111, doi:10.5194/bg-6-103-2009, 2009. 345, 357, 360, 378

Deeter, M., Emmons, L., Francis, G., Edwards, D., Gille, J., Warner, J., Khattatov, B., Ziskin, D., Lamarque, J.-F., Ho, S.-P., Yudin, V., Attie, J.-L., Packman, D., Chen, J., Mao, D., and Drummond, J.: Operational carbon monoxide retrieval algorithm and selected results for the MOPITT instrument, J. Geophys. Res., 108, D14, doi:10.1029/2002JD003186, 2003. 345, 358

Deeter, M. N., Edwards, D. P., and Gille, J. C.: Retrievals of carbon monoxide profiles from MOPITT observations using lognormal a priori statistics, J. Geophys. Res., 112, D11311,

ACPD
11, 341–386, 2011

doi:10.1029/2006JD007999, 2007. 345, 358
Deeter, M. N., Edwards, D. P., Gille, J. C., Emmons, L. K., Francis, G., Ho, S.-P., Mao, D., Masters, D., Worden, H., Drummond, J. R., and Novelli, P. C.: The MOPITT version 4 CO product: algorithm enhancements, validation, and long term stability, J. Geophys. Res., 115, D07306, doi:10.1029/2009JD013005, 2010. 345, 358
Duncan, B. N., Logan, J. A., Bey, I., Megretskaia, I. A., Yantosca, R. M., Noveli, P. C., Jones, N. B., and Rinsland, C. P.: Global budget of CO, 1988–1997: source estimates and validation with a global model, J. Geophys. Res., 112, D22301, doi:10.1029/2005JD008459, 2007. 349
Emmons, L. K., Edwards, D. P., Deeter, M. N., Gille, J. C., Campos, T., Nédélec, P., Novelli, P., and Sachse, G.: Measurements of Pollution In The Troposphere (MOPITT) validation through 2006, Atmos. Chem. Phys., 9, 1795–1803, doi:10.5194/acp-9-1795-2009, 2009. 359
Enting, I. G.: Inverse Problems in Atmospheric Constituent Transport, Cambridge University Press, Cambridge, 2002. 344
Fisher, M.: Minimization algorithms for variational data assimilation, in: ECMWF Seminar on Recent Developments in Numerical Methods for Atmospheric Modelling, ECMWF, Shinfield Park, Reading, 19998. 347
Fisher, M. and Courtier, P.: Estimating the covariance matrices of analysis and forecast error in variational data assimilation, Tech. rep., ECMWF, Shinfield Park, Reading, UK, 1995. 347
Fortems-Cheiney, A., Chevallier, F., Pison, I., Bousquet, P., Carouge, C., Clerbaux, C., Coheur, P.-F., George, M., Hurtmans, D., and Szopa, S.: On the capability of IASI measurements to inform about CO surface emissions, Atmos. Chem. Phys., 9, 8735–8743, doi:10.5194/acp-9-8735-2009, 2009. 345
Gloudemans, A. M. S., de Laat, A. T. J., Schrijver, H., Aben, I., Meirink, J. F., and van der Werf, G. R.: SCIAMACHY CO over land and oceans: 2003–2007 interannual variability, Atmos. Chem. Phys., 9, 3799–3813, doi:10.5194/acp-9-3799-2009, 2009. 357
Gonzi, S. and Palmer, P. I.: Vertical transport of surface fire emissions observed from space, J. Geophys. Res., 115, D02306, doi:10.1029/2009JD012053, 2010. 363, 379
Heald, C. L., Jacob, D. J., Jones, D. B. A., Palmer, P. I., Logan, J. A., Streets, D. G., Sachse, G. W., Gille, J. C., Hoffman, R. N., and Nehrkorn, T.: Comparative inverse analysis of satellite (MOPITT) and aircraft (TRACE-P) observations to estimate Asian sources of carbon monoxide, J. Geophys. Res., 109, D23306, doi:10.1029/2004JD005185, 2004. 345
Houweling, S., Dentener, F., and Lelieveld, J.: The impact of nonmethane hydrocarbon com-

ACPD
11, 341–386, 2011

pounds on tropospheric photochemistry, J. Geophys. Res., 103, 10673–10696, 1998. 348
Hudman, R., Murray, L., Jacob, D., Millet, D., Turquety, S., Wu, S., Blake, D., Goldstein, A., Holloway, J., and Sachse, G.: Biogenic versus anthropogenic sources of CO in the United States, Geophys. Res. Lett., 35, L04801, doi:10.1029/2007GL032393, 2008. 360
Huijnen, V., Williams, J., van Weele, M., van Noije, T., Krol, M., Dentener, F., Segers, A., Houweling, S., Peters, W., de Laat, J., Boersma, F., Bergamaschi, P., van Velthoven, P., Le Sager, P., Eskes, H., Alkemade, F., Scheele, R., Nédélec, P., and Pätz, H.-W.: The global chemistry transport model TM5: description and evaluation of the tropospheric chemistry version 3.0, Geosci. Model Dev., 3, 445–473, doi:10.5194/gmd-3-445-2010, 2010. 348, 362, 365
Jones, D. B. A., Bowman, K. W., Logan, J. A., Heald, C. L., Liu, J., Luo, M., Worden, J., and Drummond, J.: The zonal structure of tropical O_3 and CO as observed by the Tropospheric Emission Spectrometer in November 2004 – Part 1: Inverse modeling of CO emissions, Atmos. Chem. Phys., 9, 3547–3562, doi:10.5194/acp-9-3547-2009, 2009. 345, 360, 378
Kaminski, T., Rayner, P. J., Heimann, M., and Enting, I. G.: On aggregation errors in atmospheric transport inversions, J. Geophys. Res., 106, 4703–4715, 2001. 345
Kasibhatla, P., Arellano, A., Logan, J. A., Palmer, P. I., and Novelli, P.: Top-down estimates of a large source of atmospheric carbon monoxide associated with fuel combustion in Asia, Geophys. Res. Lett., 29, 1900, doi:10.1029/2002GL015581, 2002. 345, 360
Kasischke, E. S., Hyer, E. J., Novelli, P. C., Bruhwiler, L. P., French, N. H. F., Sukhinin, A. I., Hewson, J. H., and Stocks, B. J.: Influences of boreal fire emissions on Northern Hemisphere atmospheric carbon and carbon monoxide, Global Biogeochem. Cy., 19, GB1012, doi:10.1029/2004GB002300, 2005. 354
Kopacz, M., Jacob, D. J., Henze, D. K., Heald, C. L., Streets, D. G., and Zhang, Q.: Comparison of adjoint and analytical Bayesian inversion methods for constraining Asian sources of carbon monoxide using satellite (MOPITT) measurements of CO columns, J. Geophys. Res., 114, D04305, doi:10.1029/2007JD009264, 2009. 345
Kopacz, M., Jacob, D. J., Fisher, J. A., Logan, J. A., Zhang, L., Megretskaia, I. A., Yantosca, R. M., Singh, K., Henze, D. K., Burrows, J. P., Buchwitz, M., Khlystova, I., McMillan, W. W., Gille, J. C., Edwards, D. P., Eldering, A., Thouret, V., and Nedelec, P.: Global estimates of CO sources with high resolution by adjoint inversion of multiple satellite datasets (MOPITT, AIRS, SCIAMACHY, TES), Atmos. Chem. Phys., 10, 855–876, doi:10.5194/acp-10-855-2010, 2010. 345, 349, 360, 366, 378

ACPD
11, 341–386, 2011

Krol, M., Houweling, S., Bregman, B., van den Broek, M., Segers, A., van Velthoven, P., Peters, W., Dentener, F., and Bergamaschi, P.: The two-way nested global chemistry-transport zoom model TM5: algorithm and applications, Atmos. Chem. Phys., 5, 417–432, doi:10.5194/acp-5-417-2005, 2005. 348

de Laat, A. T. J., Gloudemans, A. M. S., Aben, I., and Schrijver, H.: Global evaluation of SCIAMACHY and MOPITT carbon monoxide column differences for 2004–2005, J. Geophys. Res., 115, D06307, doi:10.1029/2009JD012698, 2010. 359

Labonne, M., Bréon, F.-M., and Chevallier, F.: Injection height of biomass burning aerosols as seen from a spaceborne lidar, Geophys. Res. Lett., 34, L11806, doi:10.1029/2007GL029311, 2007. 349

Lawrence, M. G., Jöckel, P., and von Kuhlmann, R.: What does the global mean OH concentration tell us?, Atmos. Chem. Phys., 1, 37–49, doi:10.5194/acp-1-37-2001, 2001. 363

Lelieveld, J., Butler, T. M., Crowley, J. N., Dillon, T. J., Fischer, H., Ganzeveld, L., Harder, H., Lawrence, M. G., Martinez, M., Taraborrelli, D., and Williams, J.: Atmospheric oxidation capacity sustained by a tropical forest, Nature, 452, 737–740, doi:10.1038/nature06870, 2008. 365

Logan, J. A., Prather, M. J., Wofsy, S. C., and McElroy, M. B.: Tropospheric chemistry: a global perspective, J. Geophys. Res., 86, 7210–7254, 1981. 344

Meirink, J.-F., Bergamaschi, P., Frankenberg, C., d'Amelio, M. T. S., Dlugokencky, E. J., Gatti, L. V., Houweling, S., Miller, J. B., Röckmann, T., Villani, M. G., and Krol, M. C.: Four-dimensional variational data assimilation for inverse modelling of atmospheric methane emissions: analysis of SCIAMACHY observations, J. Geophys. Res., 113, D17301, doi:10.1029/2007JD009740, 2008a. 345

Meirink, J. F., Bergamaschi, P., and Krol, M. C.: Four-dimensional variational data assimilation for inverse modelling of atmospheric methane emissions: method and comparison with synthesis inversion, Atmos. Chem. Phys., 8, 6341–6353, doi:10.5194/acp-8-6341-2008, 2008b. 345, 346, 347, 350, 351, 353, 356

Müller, J.-F. and Stavrakou, T.: Inversion of CO and NO_x emissions using the adjoint of the IMAGES model, Atmos. Chem. Phys., 5, 1157–1186, doi:10.5194/acp-5-1157-2005, 2005. 345, 350

Myriokefalitakis, S., Vrekoussis, M., Tsigaridis, K., Wittrock, F., Richter, A., Brühl, C., Volkamer, R., Burrows, J. P., and Kanakidou, M.: The influence of natural and anthropogenic secondary sources on the glyoxal global distribution, Atmos. Chem. Phys., 8, 4965–4981,

ACPD
11, 341–386, 2011

doi:10.5194/acp-8-4965-2008, 2008. 349
Novelli, P. C., Masarie, K. A., and Lang, P. M.: Distributions and recent changes of carbon monoxide in the lower troposphere, J. Geophys. Res., 103, 19015–19033, 1998. 351
Novelli, P. C., Masarie, K. A., Lang, P. M., Hall, B. D., Myers, R. C., and Elkins, J. W.: Reanalysis of tropospheric CO trends: effects of the 1997–1998 wildfires, J. Geophys. Res., 108, 4464, doi:10.1029/2002JD003031, 2003. 351
Olivier, J., Peters, J., Granier, C., Pétron, G., Müller, J., and Wallens, S.: Present and future surface emissions of atmospheric compounds, POET report 2, EU project EVK2-1999-00011, RIVM, Bilthoven, 2003. 348
Olivier, J. G. J., Berdowski, J. J. M., Peters, J. A. H. W., Bakker, J., Visschedijk, A. J. H., and Bloos, J.-P. J.: Applications of EDGAR, Including a Description of EDGAR V3.0: reference database with trend Data for 1970–1995, NRP report no. 410200 051/RIVM report no. 773301 001, RIVM, Bilthoven, 2000. 348
Palmer, P. I., Jacob, D. J., Jones, D. B. A., Heald, C. L., Yantosca, R. M., and Logan, J. A.: Inverting for emissions of carbon monoxide from Asia using aircraft observations over the western Pacific, J. Geophys. Res., 108(D21), 8828, doi:10.1029/2003JD003397, 2003. 345
Palmer, P. I., Suntharalingam, P., Jones, D. B. A., Jacob, D. J., Streets, D. G., Fu, Q., Vay, S. A., and Sachse, G. W.: Using CO_2:CO correlations to improve inverse analysis of carbon fluxes, J. Geophys. Res., 111, 1–11, doi:10.1029/2005JD006697, 2006. 345
Pétron, G., Granier, C., Khattatov, B., Lamarque, J.-F., Yudin, V., Müller, J.-F., and Gille, J.: Inverse modeling of carbon monoxide surface emissions using Climate Monitoring and Diagnostics Laboratory network observations, J. Geophys. Res., 107, 4761m doi:10.1029/2001JD001305, 2002. 344, 345, 347
Pfister, G., Hess, P. G., Emmons, L. K., Lamarque, J.-F., Wiedinmyer, C., Edwards, D. P., Pétron, G., Gille, J. C., and Sachse, G. W.: Quantifying CO emissions from the 2004 Alaskan wildfires using MOPITT CO data, Geophys. Res. Lett., 32, L11809, doi:10.1029/2005GL022995, 2005. 355
Pison, I., Bousquet, P., Chevallier, F., Szopa, S., and Hauglustaine, D.: Multi-species inversion of CH_4, CO and H_2 emissions from surface measurements, Atmos. Chem. Phys., 9, 5281–5297, doi:10.5194/acp-9-5281-2009, 2009. 359, 360, 378
Rodgers, C. D.: Inverse Methods for Atmospheric Sounding, World Sci., London, UK, 2000. 346
Sanhueza, E., Dong, Y., Scharffe, D., Lobert, J., and Crutzen, P.: Carbon monoxide uptake by

ACPD
11, 341–386, 2011

temperate forest soils: the effect of leaves and humus layers, Tellus, 50, 51–58, 1998. 344
Schade, G. and Crutzen, P. J.: CO emissions from degrading plant matter, Tellus, 51(5), 909–918, 1999. 349
Seinfeld, J. H. and Pandis, S. N.: Atmospheric Chemistry and Physics: from Air Pollution to Climate Change, John Wiley and Sons, Hoboken, New Jersey, USA, 2006. 344, 349
Spivakovsky, C. M., Logan, J. A., Montzka, S. A., Balkanski, Y. J., Foreman-Fowler, M., Jones, D. B. A., Horowitz, L. W., Fusco, A. C., Brenninkmeijer, C. A. M., Prather, M. J., Wofsy, S. C., and McElroy, M. B.: Three-dimensional climatological distribution of tropospheric OH: update and evaluation, J. Geophys. Res., 105, 8931–8980, 2000. 348, 365, 386
Stavrakou, T. and Müller, J.-F.: Grid-based versus big region approach for inverting CO emissions using Measurement of Pollution in the Troposphere (MOPITT) data, J. Geophys. Res., 111, D15304, doi:10.1029/2005JD006896, 2006. 345, 353
Stavrakou, T., Müller, J.-F., De Smedt, I., Van Roozendael, M., van der Werf, G. R., Giglio, L., and Guenther, A.: Evaluating the performance of pyrogenic and biogenic emission inventories against one decade of space-based formaldehyde columns, Atmos. Chem. Phys., 9, 1037–1060, doi:10.5194/acp-9-1037-2009, 2009. 364
Tangborn, A., Stajner, I., Buchwitz, M., Khlystova, I., Pawson, S., Burrows, J., Hudman, R., and Nedelec, P.: Assimilation of SCIAMACHY total column CO observations: global and regional analysis of data impact, J. Geophys. Res., 114, D07307, doi:10.1029/2008JD010781, 2009. 345
Turquety, S., Logan, J. A., Jacob, D. J., Hudman, R. C., Leung, F. Y., Heald, C. L., Yantosca, R. M., Wu, S., Emmons, L. K., Edwards, D. P., and Sachse, G. W.: Inventory of boreal fire emissions for North America in 2004: importance of peat burning and pyroconvective injection, J. Geophys. Res., 112, D12S03, doi:10.1029/2006JD007281, 2007. 355
Val Martin, M., Logan, J. A., Kahn, R. A., Leung, F.-Y., Nelson, D. L., and Diner, D. J.: Smoke injection heights from fires in North America: analysis of 5 years of satellite observations, Atmos. Chem. Phys., 10, 1491–1510, doi:10.5194/acp-10-1491-2010, 2010. 363
van der Werf, G. R., Randerson, J. T., Collatz, G. J., Giglio, L., Kasibhatla, P. S., Arellano Jr., A. F., Olsen, S. C., and Kasischke, E. S.: Continental-scale partitioning of fire emissions during the 1997 to 2001 El Niño/La Niña period, Science, 303, 73–76, doi:10.1126/science.1090753, 2004. 344
van der Werf, G. R., Randerson, J. T., Giglio, L., Collatz, G. J., Kasibhatla, P. S., and Arellano

ACPD
11, 341–386, 2011

Jr., A. F.: Interannual variability in global biomass burning emissions from 1997 to 2004, Atmos. Chem. Phys., 6, 3423–3441, doi:10.5194/acp-6-3423-2006, 2006. 344, 349

van der Werf, G. R., Randerson, J. T., Giglio, L., Collatz, G. J., Mu, M., Kasibhatla, P. S., Morton, D. C., DeFries, R. S., Jin, Y., and van Leeuwen, T. T.: Global fire emissions and the contribution of deforestation, savanna, forest, agricultural, and peat fires (1997–2009), Atmos. Chem. Phys., 10, 11707–11735, doi:10.5194/acp-10-11707-2010, 2010. 344, 355, 362, 365, 366

Yumimoto, K. and Uno, I.: Adjoint inverse modeling of CO emissions over Eastern Asia using four-dimensional variational data assimilation, Atmos. Environ., 40, 6836–6845, 2006. 345

ACPD
11, 341–386, 2011

Table 1. Statistics of the fit for the stations used in the inversion. Bias is defined as the mean difference between observed and modeled CO mixing ratio: $\frac{1}{n}\sum_{i=1}^{n}\left(y_i^o - y_i^m\right)$. The χ^2/n defines the goodness of fit defined as $\frac{1}{n}\sum_{i=1}^{n}\left(\frac{y_i^o - y_i^m}{\sigma_i}\right)^2$. A χ^2/n value close to 1 indicates that the system is behaving well.

					Inversion cycle 1				Inversion cycle 2			
		lat	lon	alt	Bias (ppb)		χ^2/n		Bias (ppb)		χ^2/n	
ID	station name	(°)	(°)	(m a.s.l.)	prior	posterior	prior	posterior	prior	posterior	prior	posterior
ALT	Alert, Nunavut, Canada	82.45	−62.52	210.0	0.94	−1.97	6.94	3.01	2.78	0.40	7.29	1.16
ASC	Ascension Island, UK	−7.92	−14.42	54.0	3.20	0.17	5.97	3.03	3.77	−0.34	4.89	1.22
ASK	Assekrem, Algeria	23.18	5.42	2728.0	−3.94	1.21	4.22	1.64	−5.26	−1.14	3.86	0.91
AZR	Terceira Island, Azores, Portugal	38.77	−27.38	40.0	−8.10	−0.86	7.84	4.69	−6.67	−1.01	6.62	1.22
BMW	Tudor Hill, Bermuda, UK	32.27	−64.88	30.0	1.66	−1.06	3.78	1.48	1.98	−2.03	3.11	0.99
BRW	Barrow, Alaska, USA	71.32	−156.60	11.0	−0.52	16.65	6.78	3.05	−1.09	−0.24	6.77	0.91
CBA	Cold Bay, Alaska, USA	55.20	−162.72	25.0	−9.65	0.06	9.04	2.70	−4.33	−0.01	6.96	1.15
CGO	Cape Grim, Tasmania, Australia	−40.68	144.68	94.0	9.18	1.97	1.24	0.37	9.18	2.20	1.24	0.34
CHR	Christmas Island, Republic of Kiribati	1.70	−157.17	3.0	8.79	0.54	4.02	1.58	9.45	0.34	3.86	1.13
CRZ	Crozet Island, France	−46.45	51.85	120.0	5.84	−0.28	3.87	1.14	5.52	−0.20	3.69	0.91
EIC	Easter Island, Chile	−27.15	−109.45	50.0	−9.03	−9.07	5.64	5.26	0.73	−3.07	0.46	1.92
GMI	Mariana Islands, Guam	13.43	144.78	6.0	−8.19	−4.07	4.30	3.23	−1.74	−0.49	2.80	1.32
HBA	Halley station, Antarctica, UK	−75.58	−26.50	33.0	6.93	0.04	4.33	0.65	6.93	0.09	4.33	0.57
ICE	Heimay, Vestmannaeyjar, Iceland	63.25	−20.15	100.0	−0.88	0.97	5.02	1.80	−1.71	−0.22	4.84	1.08
IZO	Izana, Canary Islands, Spain	28.30	−16.48	2360.0	−2.66	−1.45	4.74	2.17	−2.92	−2.66	3.84	1.28
MHD	Mace Head, Ireland	53.33	−9.90	25.0	3.98	2.98	1.60	0.87	4.64	4.02	1.55	0.73
MID	Sand Island, Midway, USA	28.21	−177.38	7.7	−14.07	−0.63	10.26	3.88	−13.81	−0.26	9.74	1.49
MLO	Mauna Loa, Hawaii, USA	19.53	−155.58	3397.0	−3.51	−1.87	3.53	2.47	−0.45	−0.78	2.18	1.28
NWR	Niwot Ridge, Colorado, USA	40.05	−105.58	3526.0	−4.05	2.13	3.13	2.50	−0.88	2.72	2.58	1.22
PAL	Pallas, Finland	67.97	24.12	560.0	−1.88	−3.22	4.08	1.63	−0.19	1.51	3.80	0.81
PSA	Palmer Station, Antarctica, USA	−64.92	−64.00	10.0	6.62	−0.20	3.74	0.63	6.52	0.04	3.74	0.61
RPB	Ragged Point, Barbados	13.17	−59.43	45.0	7.13	0.55	3.85	2.08	7.36	−0.12	3.50	1.13
SEY	Mahe Island, Seychelles	−4.67	55.17	7.0	3.84	0.85	3.41	1.75	5.60	0.75	3.08	0.99
SHM	Shemya Island, Alaska, USA	52.72	174.10	40.0	−7.16	−0.29	9.16	3.24	−2.21	0.77	7.96	1.05
SMO	Cape Matatula, Tutuila, American Samoa	−14.24	−170.57	42.0	4.67	0.28	2.48	1.23	5.06	−0.02	2.36	1.04
SPO	South Pole, Antarctica, USA	−89.98	−24.80	2810.0	6.82	0.50	4.50	1.08	6.60	0.35	4.36	1.01
STM	Ocean station M, Norway	66.00	2.00	5.0	0.36	−0.06	6.67	1.98	1.76	0.23	6.39	1.08
SYO	Syowa Station, Antarctica, Japan	−69.00	39.58	14.0	6.52	0.25	3.81	0.57	6.52	0.17	3.81	0.51
TDF	Tierra del Fuego, La Redonda Isla, Argentina	−54.87	−68.48	20.0	5.89	−0.75	3.73	0.66	5.89	−0.53	3.73	0.60
WLG	Mt. Waliguan, Peoples Republic of China	36.29	100.90	3810.0	−33.31	0.18	19.22	4.27	−21.26	−0.32	13.77	1.03
ZEP	Ny-Alesund, Svalbard, Spitsbergen	78.90	11.88	475.0	1.57	1.76	9.94	3.31	−3.10	0.29	7.69	1.11
ALL					−0.58	0.46	5.54	2.17	1.53	0.21	4.55	1.00

ACPD
11, 341–386, 2011

Table 2. Emissions for 2003 and 2004 per continent for three surface source categories (Anthropogenic, Biomass burning and Natural) and two global chemical production terms (methane and NMVOCs). Per source category, the left column is the a priori annual emission for the corresponding continent, the right column specifies the a posteriori emission. The emissions are given in Tg CO yr^{-1}. Note that the sources of CO production from methane and NMVOC oxidation are given as global totals only, since only a global scaling factor is adjusted.

Region	Anthropogenic		Biomass Burning		Natural		CH_4-CO		NMVOC-CO	
2003	prior	posterior	prior	posterior	prior	posterior	prior	posterior	prior	posterior
Nam	105±30	85±27	32±32	61±30	15±8	12±8	–	–	–	–
Sam	22±16	−9±16	60±48	75±37	18±13	8±12	–	–	–	–
Europe	62±30	67±16	3±2	6±2	4±4	6±4	–	–	–	–
Africa	80±52	124±48	162±91	85±72	21±12	29±12	–	–	–	–
Asia	258±150	497±82	114±81	158±38	30±12	30±12	–	–	–	–
Oceania	5±1	5±1	24±28	13±11	8±6	5±6	–	–	–	–
Globe	531±184	770±71	397±138	400±88	115±24	101±24	885±10	883±10	812±40	574±38
2004	prior	posterior	prior	posterior	prior	posterior	prior	posterior	prior	posterior
Nam	105±30	105±26	23±19	47±10	15±8	14±8	–	–	–	–
Sam	22±16	0±16	98±105	136±39	18±13	19±12	–	–	–	–
Europe	62±30	85±18	2±1	3±1	4±4	5±4	–	–	–	–
Africa	80±52	149±45	165±94	165±63	21±12	25±12	–	–	–	–
Asia	258±150	526±75	98±65	42±41	30±12	29±11	–	–	–	–
Oceania	5±1	4±1	18±14	16±14	8±6	6±6	–	–	–	–
Globe	531±184	871±77	404±157	409±76	115±24	111±24	885±10	887±10	812±40	410±36

ACPD
11, 341–386, 2011

Table 3. Comparison of prior (left columns) and posterior (right columns) continental emission estimates for 2004 of this study with four recent studies. Numbers are the sum of anthropogenic, biomass burning and natural emissions given in Tg CO yr^{-1}.

Region	This study		Pison et al. (2009)		Kopacz et al. (2010)		Jones et al. (2009)		Chevallier et al. (2009)	
	prior	posterior	prior	posterior	prior	posterior	prior	posterior	prior	posterior
Nam	142±37	167±25	137	188	57	71	135	165	–	–
Sam	138±107	156±39	146	131	119	183	113	157	–	–
Europe	67±30	92±17	103	128	78	95	110	111	–	–
Africa	266±108	338±74	264	317	214	343	234	359	286	255
Asia	385±212	597±98	296	539	389	660	367	483	–	–
Oceania	31±15	26±15	96	88	23	41	69	165	–	–
Total	1030	1374	1042	1391	880	1393	1028	1440	–	–

ACPD
11, 341–386, 2011

Table 4. Summary of the 7 sensitivity studies to investigate the influence of prior information, error settings and model errors on the inversion results.

Study	Description
S1	Prior grid-scale surface emission uncertainty doubled
S2	Prior grid-scale surface emission uncertainty halved
S3	Prior uncertainty on NMVOC-CO source 16% (8% in the base inversion)
S4	Prior uncertainty on NMVOC-CO source 4%
GFED3.1	Use GFED3.1 as biomass burning inventory
OH	Use the OH field from a full-chemistry simulation with TM5
FVERT	Use vertical distribution of biomass burning following Gonzi and Palmer (2010)

ACPD
11, 341–386, 2011

Table 5. Prior and posterior global emission estimates (in Tg CO yr^{-1}) for 2004 and their uncertainty for the sensitivity studies.

	ANT		BB		NMVOC-CO	
	APRI	APOS	APRI	APOS	APRI	APOS
Base	531±183	871±77	404±157	409±76	812±41	410±36
S1	531±364	804±130	404±314	430±138	812±41	520±36
S2	531±94	879±40	404±79	455±48	812±41	362±36
S3	531±183	935±78	404±157	477±89	812±81	293±72
S4	531±183	753±72	404±157	400±74	812±20	581±20
GFED3.1	531±183	932±73	334±119	365±71	812±41	433±36
OH	531±183	967±74	404±157	321±73	812±41	369±36
FVERT	531±183	850±69	404±157	484±76	812±41	403±36

ACPD
11, 341–386, 2011

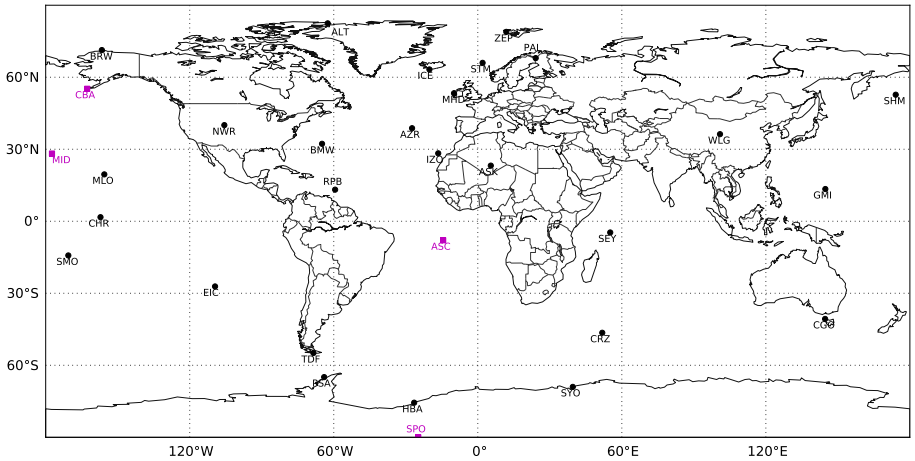

Fig. 1. Positioning of 31 NOAA surface sites (black circles). Purple squares represent stations for which prior and posterior simulations will be shown (Sect. 3.1).

ACPD
11, 341–386, 2011

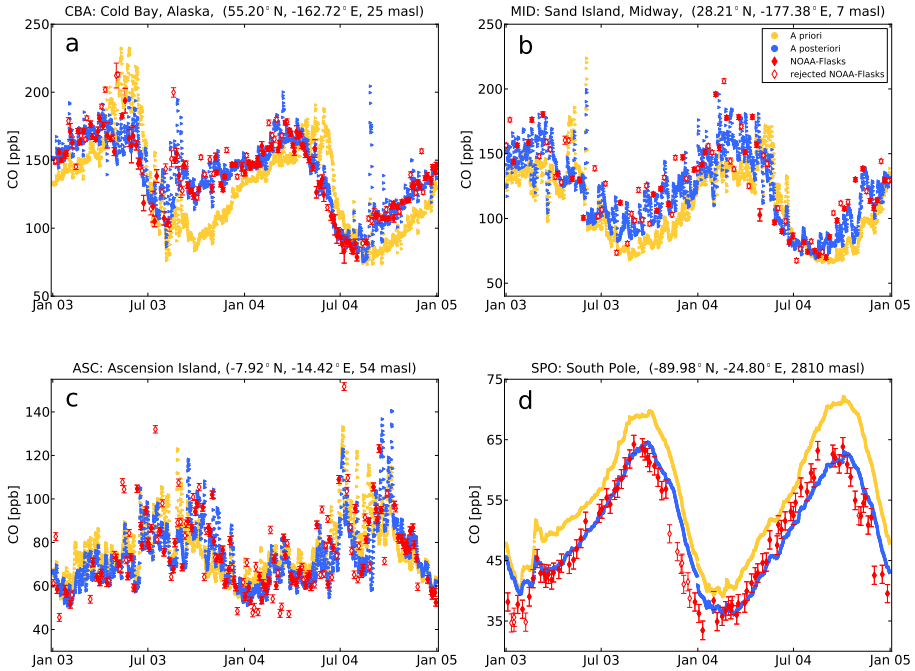

Fig. 2. Comparison of modeled and observed CO mixing ratios at 4 stations of the NOAA surface network. Red dots correspond to NOAA observations, red open markers represent rejected data from inversion cycle 1 to cycle 2. Model simulations using prior (posterior) settings are shown in yellow (blue).

ACPD
11, 341–386, 2011

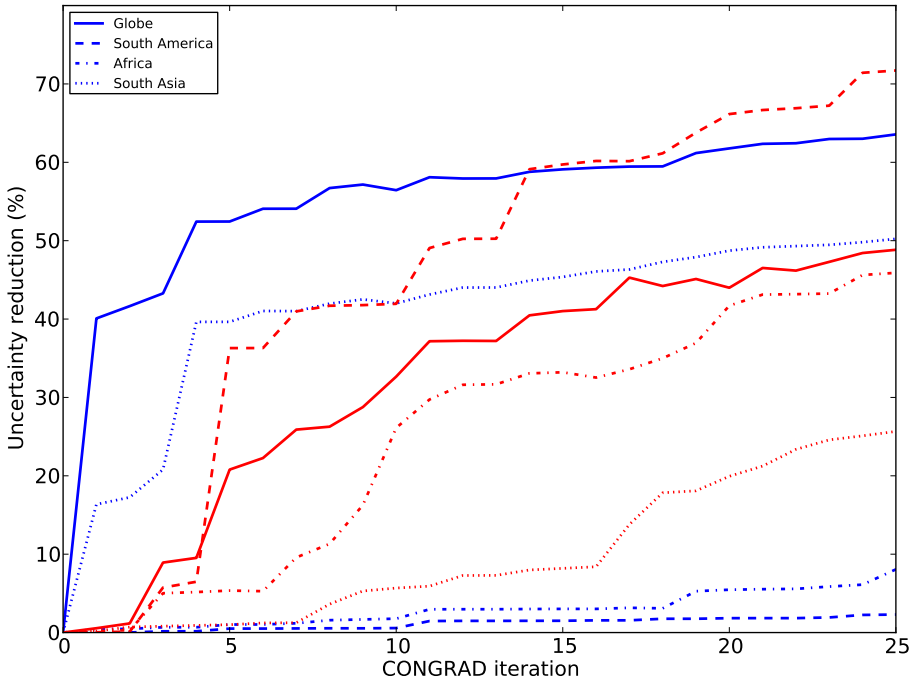

Fig. 3. Uncertainty reduction for 2004, defined as $1-\frac{\sigma_a}{\sigma_b}$, where σ_a (σ_b) is the aggregated posterior (prior) uncertainty for the anthropogenic emissions (blue) and biomass burning emissions (red) for four large regions as a function of the iteration number in CONGRAD. A convergence criterium of 99% gradient norm reduction is used here.

ACPD
11, 341–386, 2011

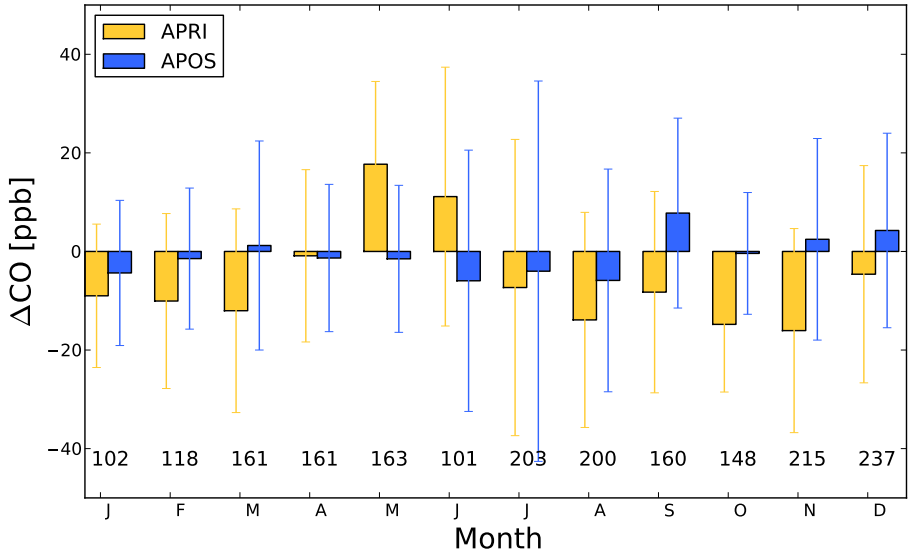

Fig. 4. Monthly mean difference between the TM5 model and NOAA aircraft observations for the prior (yellow) and posterior (blue) simulation. The number of observations per month is also given.

ACPD
11, 341–386, 2011

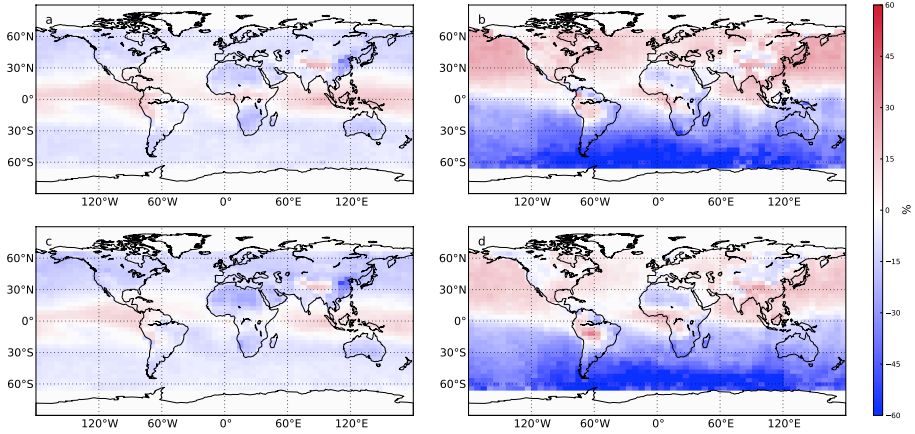

Fig. 5. Annual difference in CO total column, TM5-MOPITT relative to TM5 (%) for the years 2003 (top) and 2004 (bottom). Modeled CO total columns are derived using the prior (left) and posterior (right) emissions. Reddish colors indicate higher TM5 CO total columns compared to MOPITT and blueish colors indicate a lower modeled CO total column compared to MOPITT.

ACPD
11, 341–386, 2011

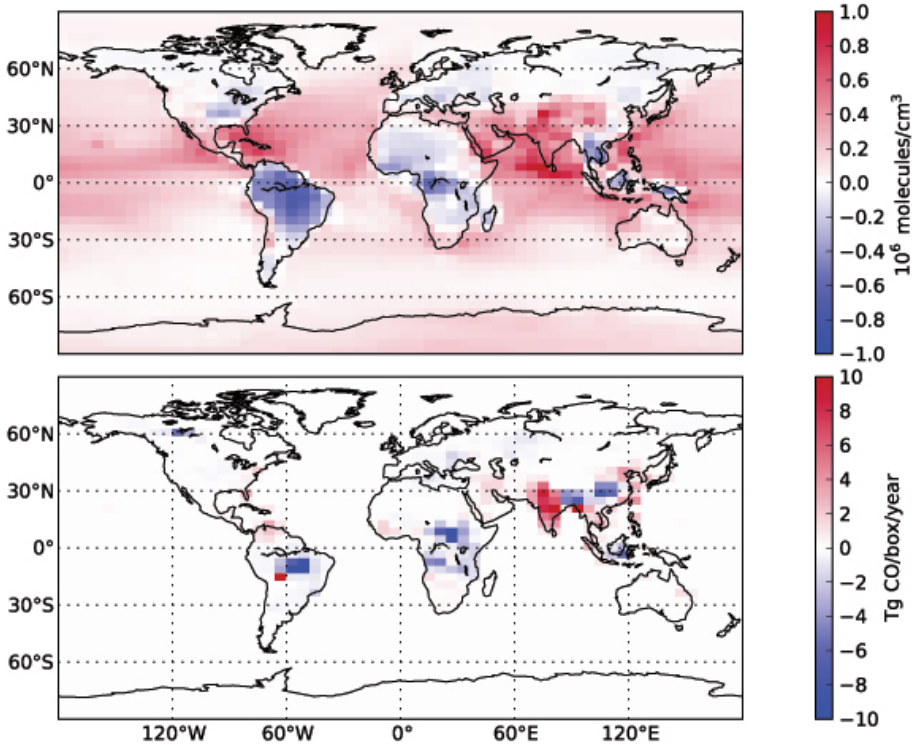

Fig. 6. Top: Vertically integrated mass- and rate constant weighted OH difference field (TM5 – Spivakovsky et al., 2000). Bottom: Emission increments difference for 2004, OH – Base. Reddish colors indicate higher OH levels in the TM5 OH field compared to the OH field from Spivakovsky et al. (2000) (top) and increased emissions with respect to the base inversion (bottom). Blueish colors indicate lower OH levels (top) and decreasing emissions (bottom).

ACPD
11, 341–386, 2011